Nanoscale

ROYAL SOCIETY OF CHEMISTRY

PAPER

View Article Online
View Journal | View Issue

Cite this: *Nanoscale*, 2021, **13**, 9881

All-boron planar ferromagnetic structures: from clusters to monolayers†

Chang-Chun He,[a,b] Shao-Gang Xu,[b] Yu-Jun Zhao,[a] Hu Xu*[b] and Xiao-Bao Yang*[a,c]

Received 15th February 2021,
Accepted 8th May 2021

DOI: 10.1039/d1nr00981h

rsc.li/nanoscale

Ferromagnetism in all-boron planar clusters is revealed based on high-throughput first-principles calculations. Magnetic boron clusters induced from p electrons have been confirmed with large spins, *e.g.*, S = 3 in a B_{34} cluster, which can be assembled to construct all-boron ferromagnetic monolayers. Notably, the ferromagnetic semiconductors of boron monolayers can be designed with the hybridization of a non-magnetic B_{36} cluster in experimental synthesis. The ferromagnetism–paramagnetism transition and semiconductor–metal transition in these boron nanostructures will occur around 500 K according to *ab initio* molecular dynamics simulation, indicating the potential applications in nano-devices at room temperature. The coexisting ferromagnetic and semiconducting properties in boron monolayers are attributed to the unique multicenter bonds together with the modulation of structural symmetry, which might be worth experimental attempts in the future.

1 Introduction

Magnetic materials have opened the opportunity to synthesize unconventional spintronic devices, which are superior to charge-based devices with higher efficiency of energy utilization and faster speed of data processing.[1] In addition, magnetism in two-dimensional (2D) materials has been particularly attractive in both theory[2] and experiment[3] due to the rapid development for applications in practical spintronic devices.[4] Compared with the magnetism in bulk derived from d electrons of transition metal elements, metal-free spintronic devices derived from sp electrons can be more environmentally friendly, which are biocompatible for human health with lower electric power consumption.[5] An early experiment has demonstrated that magnetism can arise from only p electrons in the carbon π-electron system at room temperature,[6] indicating the promising future of metal-free systems in the next-generation information devices.

In theoretical investigations, the topological frustration in graphene nanoflakes has been predicted to induce the antiferromagnetic (AFM) order for spin logic devices,[7] and the rules for the exchange interactions in π-conjugated hydrocarbon systems have been recently provided.[8] The magnetic order has been confirmed by successive experiments in these graphene clusters with various shapes and sizes.[9–11] Consisting of a single pentagonal ring in a benzenoid framework, the non-benzenoid topological defect in nanographene will also induce unpaired π-electrons,[12] while two spins in the covalently linked nanographene dimers are antiferromagnetically coupled with each other as confirmed by inelastic spin–flip excitation spectroscopy and the mean-field Hubbard model calculations.[13] With the introduction of nitrogen (N),[14,15] *g*-C_4N_3 with the kagome lattice has been predicted to maintain the ferromagnetic order at room temperature,[16] while a family of 2D C_nN_m sheets is found to be either semiconducting or ferromagnetic tuned through external strain.[17]

As the neighborhood of carbon in the element periodic table, boron has a particularly complex potential energy surface due to electron deficiency,[18] where the p electrons in the π orbitals are dominant to the stabilities and properties.[19] Besides planar B_{36} with the C_{6v} symmetry,[20] various boron planar clusters with hexagonal vacancies have been synthesized experimentally[21–24] during the past decades. Intriguing mechanical, electronic and chemical properties have been comprehensively uncovered in low-dimensional boron;[25] the 2D semimetallic boron allotrope with massless Dirac fermions was predicted based on an *ab initio* evolutionary structure search,[26] and superconducting[27] and semiconducting[28] characteristics are also revealed in 2D boron sheets. The thin film composed of B_{20} clusters in the hexagonal

[a]Department of Physics, South China University of Technology, Guangzhou 510640, P. R. China. E-mail: scxbyang@scut.edu.cn
[b]Department of Physics & Institute for Quantum Science and Engineering and Guangdong Provincial Key Laboratory of Computational Science and Material Design, Southern University of Science and Technology, Shenzhen 518055, P. R. China. E-mail: xuh@sustech.edu.cn
[c]Guangdong Provincial Key-lab for Computational Science, Shenzhen 518000, P. R. China

†Electronic supplementary information (ESI) available. See DOI: 10.1039/D1NR00981H

arrangement is predicted to be ferromagnetic,[29] as well as a multilayer boron sheet from the evolutionary algorithm.[30] Boldyrev *et al.* predicted that superoctahedral two-dimensional metallic boron assembled by the B6 structure can exhibit peculiar magnetic properties, among which the magnetism can be attributed to the presence of two unpaired delocalized bonding elements inside every distorted octahedron.[31] However, the magnetism of boron clusters or monolayers has not been found to date. In our previous study,[32] we have proposed a bond-distribution model to describe the structural stabilities of boron nanostructures based on competition of the 8-electron rule and the electron delocalization. With the unique multi-center bonding modulated by the structural symmetry, there will be unpaired p electrons that might further induce the magnetism in 2D boron nanostructures.

In this work, we have theoretically explored the boron planar clusters and monolayers with magnetic properties, in which the unpaired electrons are induced due to the competition of the 8-electron rule and the electron delocalization. High-throughput first-principles calculations show that ferromagnetism (FM) will occur in all-boron planar clusters, which can be further assembled to form magnetic monolayers and magnetic semiconductors depending on the motifs and the corresponding ratios. Surprisingly, the planar magnetic cluster B_{34} is found to have a large quantum spin number $S = 3$, and *ab initio* molecular dynamics (AIMD) simulation shows that the magnetic moment is still larger than $4\mu_B$ at a temperature of 500 K. In boron monolayers assembled by magnetic and nonmagnetic clusters, the magnetic semiconducting characteristics will be maintained at room temperature, indicating the robustness of the intrinsic ferromagnetic order for practical applications in novel nano-devices.

2 Method

To investigate the magnetism in boron planar nanostructures, we have used the first-principles calculations based on density functional theory implemented in Vienna *ab initio* simulation package (VASP).[33,34] The total energies are obtained by the projector augmented wave (PAW) method applied with the Perdew–Burke–Ernzerhof (PBE) functional of the Generalized Gradient Approximation (GGA).[35,36] With an energy cutoff of 480 eV, the structures were fully relaxed until the forces were less than 0.01 eV $Å^{-1}$ for all atoms, where the vacuum distance was carefully tested and set to be 12 Å to avoid cell-to-cell interactions. For boron monolayers, the Brillouin zone was sampled with allowed spacing among *k*-points less than 0.1 $Å^{-1}$, with a Γ-centered Monkhorst–Pack *k*-point grid for high-throughput calculations. Spin-polarized calculations were adopted to confirm the FM in boron nanostructures, where the possible magnetic moments are screened to determine the ground state, including various antiferromagnetic configurations for boron clusters and monolayers. In addition, the Heyd–Scuseria–Ernzerhof (HSE06)[37,38] calculation with higher accuracy was performed to confirm the structural stability of the boron clusters and monolayers with novel properties. A smaller energy convergence criterion (10^{-6} eV), a larger energy cutoff (520 eV) and a denser *k*-mesh are employed to maintain the accuracy. To check the dynamic stability of the predicted structures, we calculated the phonon dispersion and performed the *ab initio* molecular dynamics (AIMD) simulation to demonstrate the stability of these predicted magnetic monolayers. Due to the expensive computational cost, we calculated the phonon frequency for the small system. Phonon dispersion was calculated using the Phonopy code[39] with a 3 × 3 × 1 supercell.

The experimental observations[20,22] and theoretical studies[32,40] indicate that stable boron clusters are mostly triangular lattice fragments with hexagonal vacancies. According to the flowchart shown in Fig. 1, we screened the possible boron clusters and designed the corresponding monolayers as follows: (I) generate the triangular lattice fragment with the hexagonal vacancies; (II) confirm the FM in boron clusters based on the first-principles calculations; (III) assemble the clusters with large spins to construct the magnetic monolayers; and (IV) hybridize the non-magnetic and magnetic clusters to explore the ferromagnetic semiconductors of boron monolayers.

For a given triangular fragment, any two vacancies cannot be nearest-neighbor to maintain the hexagonal shape of the vacancies. We applied structural recognition to avoid repeated calculations, and the candidates with high symmetry were enumerated. When assembling the clusters (one or two motifs) into monolayers, we considered the 2D triangular and hexagonal lattices, as well as the orientation of the clusters. In such a case, we should adopt various possible supercells of a given lattice and enumerate the possible orientations of clusters, which is similar to the alloy structures. All these procedures were performed using the Structures of Alloy Generation and Recognition (SAGAR) code,[41] which was devel-

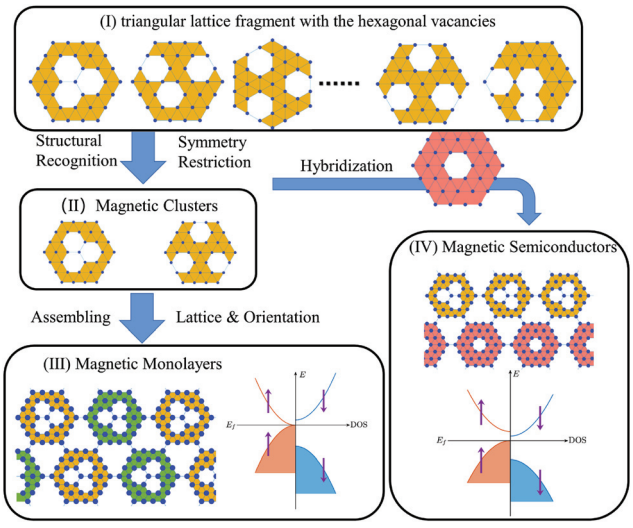

Fig. 1 The flowchart of exploring magnetic boron clusters and monolayers.

oped by our group. Finally, the all-boron monolayers with a large magnetic moment and ferromagnetic semiconducting characteristics were revealed.

3 Results and discussion

After the structural recognition, we enumerated all unique boron clusters with high symmetry (shown in the inset of Fig. 2a), in which there are 3, 5 and 5, 7, 9 vacancies in the B_{37} and B_{61} triangular fragments, respectively. The number of valence electrons is even in all these boron clusters, and the unpaired electrons are not as trivial as in the case of dangling bonds. The results show that the structural symmetry plays an important role in inducing the unpaired electrons in boron clusters because 76.7% of these symmetric boron clusters exhibit net magnetic moments. For comparison, boron clusters with no symmetry are generated by a random distribution of hexagonal vacancies, most of which are energetically favorable at the nonmagnetic state (shown in Fig. 2a). Note that the proportion of boron clusters with total spin numbers S of 3 and 4 is only 8%, corresponding to the structures with high symmetry.

Among the structures with the same spin number, magnetic boron clusters with the lowest energy are shown in Fig. 2b. In particular, B_{34} (S = 3) and B_{52} (S = 4) both belong to the C_{3v} point group, as shown in Fig. 2b, where local magnetization is mainly distributed at the edge of the structures. The spin orientation of the vertex sites of the boron convex hull is aligned parallel, which is similar to the case of graphene nanoflakes[42] which is consistently verified by experimental observation.[43] The electron density distribution must be consistent with the symmetry of the structures. However, the 8-electron rule may not be satisfied, and unpaired electrons occur. To confirm the FM in these boron clusters, hundreds of AFM configurations are generated according to the structural symmetry, where the equivalent atomic sites should have the same spin orientation. The minimum energies of these four AFM clusters are 4.88, 99.97, 24.37, and 6.31 meV μ_B^{-1} larger than that of FM, which are the average energy difference per magnetic moment. In addition, HSE calculations also indicate that the energies of the AFM states are 15.79, 45.47, 27.31, and 1.86 meV μ_B^{-1} higher than that of the FM state, confirming the ground state of FM. Furthermore, we have systematically compared the total energy between the predicted magnetic boron clusters in Fig. 2b and the proposed boron clusters in previous works, as presented in Table S1 of the ESI.† Although the freestanding magnetic boron clusters are not energetically favorable compared to the boron clusters which is confirmed in previous theoretical and experimental works,[44,45] it is demonstrated that these magnetic boron clusters will become more stable on suitable metal substrates (Ag(111), Cu(111), Au (111)) according to our calculations as shown in Fig. S2 of the ESI.† This indicates that the synthesis of these magnetic boron clusters is possible on suitable substrates experimentally.

To investigate the thermodynamic properties of the magnetic clusters, we performed the AIMD simulation on B_{34} (S = 3) and B_{52} (S = 4), where the time-average magnetic moments (each over 5 ps) at various temperatures are shown in Fig. 3a. The FM of B_{34} is found to be robust because a magnetic moment larger than $4\mu_B$ still remains after 5 ps even at 500 K,

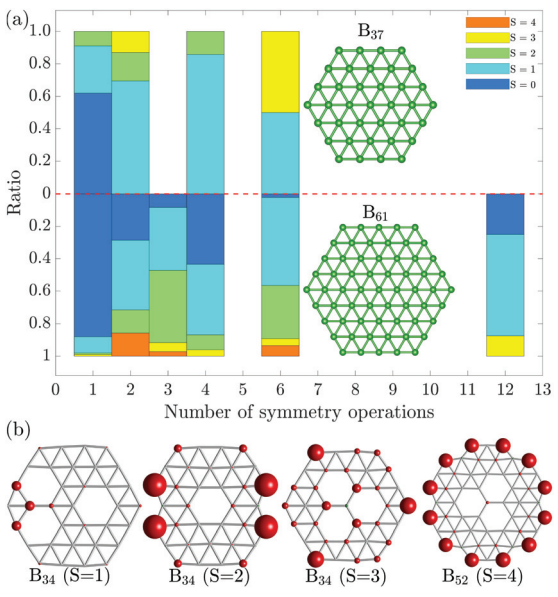

Fig. 2 (a) The ratio of boron clusters with various spin numbers as a function of symmetry operations. The up/down part is based on the B_{37}/B_{61} cluster. (b) The distribution of the magnetic moment in the boron clusters with S = 1, 2, 3, 4.

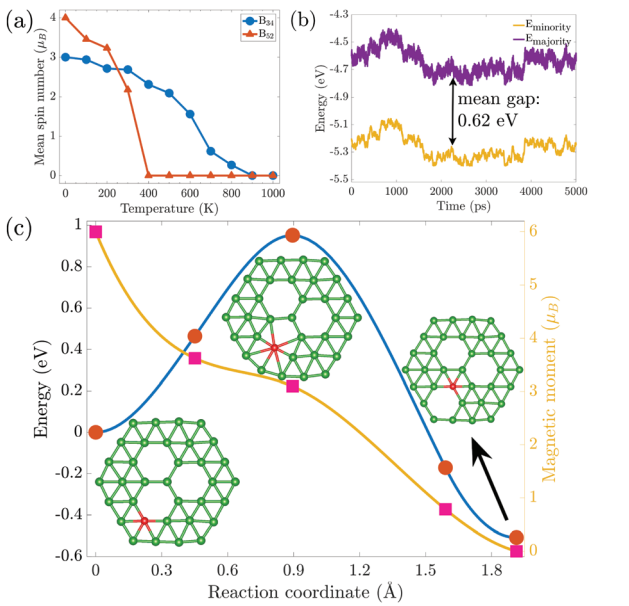

Fig. 3 (a) The time-average magnetic moment at various temperatures of the B_{34} and B_{52} cluster, respectively; the spin charge density of B_{34} and B_{52} are shown in the inset. (b) The $E_{majority}$ and $E_{minority}$ fluctuation of B_{34} at room temperature of 300 K. (c) The energy barrier and magnetic moment of the magnetic B_{34} cluster to a nonmagnetic B_{34} cluster; the moved atom is marked in red.

while B_{52} does not exhibit a ferromagnetic state above 400 K due to the drastic atomic vibration. This difference also indicates that the edge hexagonal vacancies will significantly decrease the stability.[46] To distinguish from other B_{34} isomers, the one with $S = 3$ is designated as α-B_{34}. For the α-B_{34} cluster, there are six unpaired electrons at the majority spin orbitals and six corresponding empty orbitals at the minority spin orbitals, whose mean energy levels are marked as $E_{majority}$ and $E_{minority}$, respectively (the exact definition is described in the section Calculation details of $E_{majority}$ and $E_{minority}$ of the ESI†). At $T = 300$ K, both $E_{majority}$ and $E_{minority}$ will fluctuate as a function of time as shown in Fig. 3b. There is still an apparent gap of 0.62 eV, indicating that the α-B_{34} cluster can well maintain the magnetic characteristics at room temperature. The gap will gradually vanish at high temperatures, and the FM state will also disappear. To confirm the dynamic stability of the α-B_{34} cluster, we constructed a series of transition state images[47] by exchanging boron atoms and vacancies, which results in another B_{34} cluster with a lower energy and zero magnetic moment (as shown in Fig. 3c). Although this moved boron atom will not dramatically affect the spin charge density of the upper right part of the B_{34} cluster, as shown in Fig. S3 of the ESI,† the disappearance of magnetism might be caused by the symmetry breaking of the α-B_{34} cluster, which makes the electronic configuration with spin polarization become unstable. However, there is an energy barrier of about 1 eV in the reaction path, indicating that the α-B_{34} cluster is a metastable structure with ferromagnetic characteristics.

The above results and discussions show that α-B_{34} is a stable boron cluster with large spins, which might be assembled to construct the ferromagnetic monolayers. With the symmetry of the C_{3v} point group, we can easily select the planar triangular lattice with one cluster in the unit cell (as shown in Fig. 4a), which is found to be ferromagnetic with the magnetic moment $M = 2\mu_B$ per cluster. Compared with the isolated α-B_{34} cluster, the magnetic moment in the monolayer is mainly distributed on the central B atom with three nearest neighbors, rather than the edge. Note that the orientation of α-B_{34} is important, which will dramatically modulate the magnetic moments of the monolayer. As shown in Fig. 4b, there is a reversed α-B_{34} cluster in a six times larger supercell, which will significantly decrease the magnetic moment on the clusters around the reversed one. As a result, the magnetic moment per cluster in this monolayer is reduced from $2.00\mu_B$ to $1.20\mu_B$.

For a given supercell of the triangular lattice, the number of reversed α-B_{34} is defined as type-I, and the possible supercells with various distributions have been enumerated using SAGAR.[41] As shown in Fig. 4c, the maximum magnetic moments at each rate of orientation type-I almost linearly decrease with the rate, which suggests that the reverse orientation of α-B_{34} will efficiently decrease the magnetic moment in a triangular lattice. To demonstrate the effect of the reversed α-B_{34} distribution, we consider the correlations of α-B_{34} with the same direction as a function of distance, in which S_I, S_{II}, and S_{III} correspond to the nearest/next-nearest/third-nearest neighboring correlations, respectively. According to the linear regression (shown in Fig. 4), the magnetic moment M can be expressed as follows: $M = c_0 + c_1 \times S_I + c_2 \times S_{II} + c_3 \times S_{III}$, where the regression coefficients ($c_1 = 1.34$, $c_2 = 0.99$, $c_3 = 0.43$) are determined by the least-squares method. All these positive coefficients indicate that the same orientation will enhance the magnetic moment, in which the correlation decreases with the distance of clusters.

In the triangular lattice, the monolayer assembled from α-B_{34} possesses the maximum magnetic moment when all the clusters are in the same orientation (shown in Fig. 4a), where $E_{FM} - E_{AFM} = -6.19$ meV μ_B^{-1}. However, in the hexagonal lattice, the magnetic moment is smaller for all the clusters in the same orientation (shown in Fig. 5a), compared with the one where all the nearest neighboring clusters are the reversed ones (shown in Fig. 5b). These two monolayers are ferromagnetic, where $E_{FM} - E_{AFM} = -18.50$ and -23.91 meV μ_B^{-1}, respectively. Fig. 5c shows that the magnetic moment per cluster increases with the rate of reversed clusters. For the monolayers with half reversed clusters, the magnetic moment per cluster will vary from $2.00\mu_B$ to $2.80\mu_B$, depending on the distribution of clusters with different orientations.

This different magnetic nature between the triangular lattice case and the hexagonal lattice case can be understood by the local magnetization distribution of the isolated α-B_{34} cluster, which is mainly distributed at the edge Q sites (shown in the inset of Fig. 5c). When P sites are bonded with P sites, the local magnetization distribution of α-B_{34} in the hexagonal lattice will retain that of the isolated α-B_{34} cluster, which will not induce the redistribution of magnetization and weaken the magnetic moment of the assembled monolayers. As shown in Fig. 5b, this monolayer has the largest magnetic moment because all the α-B_{34} clusters are bonded with P sites, maintaining the magnetization distribution of the isolated α-B_{34} cluster. To investigate the relationship between the magnetic moment and orientation of α-B_{34} clusters, we define the rate κ

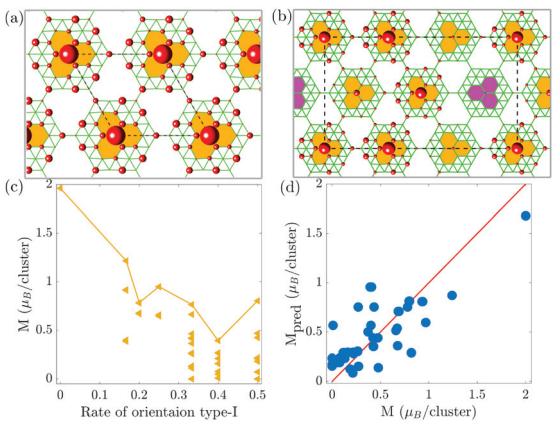

Fig. 4 The radius/blue sphere represents spin up/down. (a)/(b) In the triangular lattice, the assembled boron monolayers with the rate of type-I at 0, $\frac{1}{6}$, respectively. (c) The magnetic moment varies with the rate of type-I. (d) The relationship between the magnetic moment predicted by a linear model and magnetic moment based on DFT calculations.

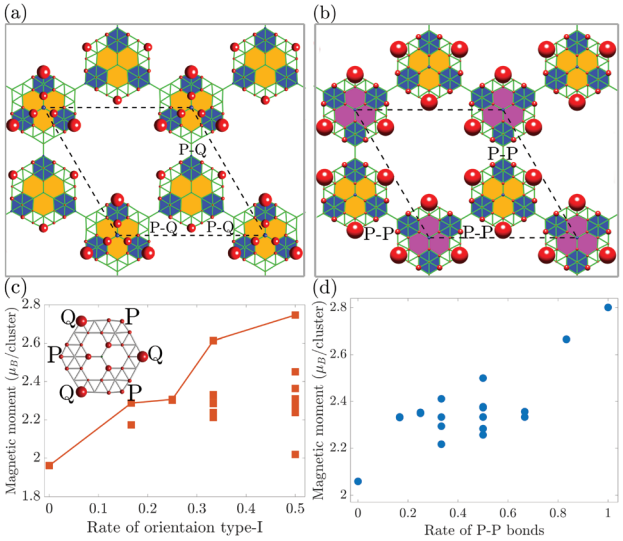

Fig. 5 (a)/(b) In the hexagonal lattice, the assembled boron monolayers with the rate of type-I at 0, $\frac{1}{2}$, respectively. (c) The magnetic moment varies with the rate of type-I. (d) The relationship between the magnetic moment and the rate κ of P–P bonds.

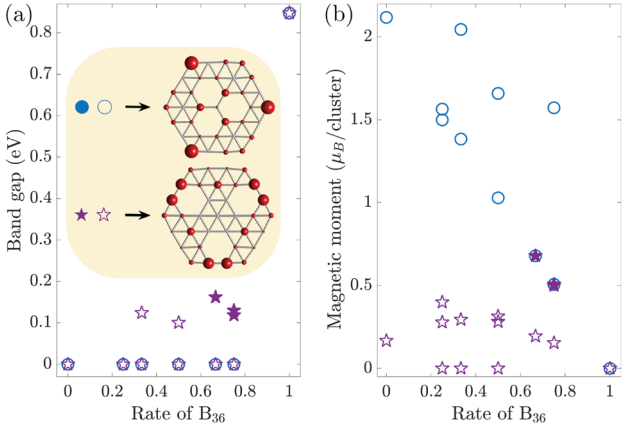

Fig. 6 (a)/(b) The magnetic moment/band gap varies with the rate of B_{36} clusters in the assembled monolayer. The circles/pentagrams represent B_{34} of type-I/II, respectively. The hollow/solid circles and pentagrams mean this structure is/is not a magnetic semiconductor.

of P–P bonds, which is 0/1 for the structures in Fig. 5a/b, respectively. For the assembled monolayers with κ from 0 to 1, the corresponding magnetic moment varies from 2.05μ_B to 2.80μ_B (shown in Fig. 5d), indicating a strong positive correlation between the rate κ and the magnetic moment. In addition, we also systematically performed the comparison of the cohesive energy between these predicted magnetic boron monolayers and the proposed boron monolayers in previous works,[48] with the calculation details presented in Table S2 of the ESI.† Furthermore, we calculated the AIMD at room temperature and the phonon dispersion of the structures as shown in Figs. 4a, b, 5a and b to confirm the dynamic stability of these predicted structures, as shown in Fig. S4–S6 of the ESI.†

After the cluster assembling, most magnetic boron monolayers are found to be metallic or half-metallic. However, is it possible to design all-boron ferromagnetic semiconducting monolayers? In the following, we will explore the magnetic semiconducting boron monolayers using the assembled clusters. According to the experiments[20] and theoretical calculations,[22] the stable B_{36} cluster belongs to the C_{6v} point group with a large energy gap of 3.5 eV, and the corresponding triangular monolayer with its assembling is nonmagnetic semiconducting with a gap of 0.84 eV. The magnetic moment will be induced when part of B_{36} clusters is substituted by α-B_{34}. However, the gap dramatically decreases to near zero, as shown by the circles of Fig. 6a. In the screening of boron clusters, we have found another B_{34} (designated as β-B_{34}) of the C_{3v} point group with S = 1, which can induce a larger band gap and maintain the magnetic properties in hybridized monolayers (plotted using solid pentagrams in Fig. 6).

Among the hybridized monolayers, the one in the absence of the B_{36} cluster has the largest magnetic moment, whereas the band gap of the monolayer without the B_{34} cluster is the largest. Interestingly, the monolayer assembled by pure β-B_{34} only exhibits a weak half-metallic state (shown in Fig. 6b), while the introduction of the B_{36} cluster will increase the magnetic moment. At some specific distribution and concentration of B_{36} and β-B_{34} clusters, the magnetic semiconductors of all-boron monolayers are recovered.

Among these monolayers, we have found a monolayer with a band gap of 0.18 eV and a magnetic moment of 0.68μ_B per cluster, as shown in the inset of Fig. 7a. In particular, we designate this magnetic semiconductor boron monolayer as MS-boron, in which there are two B_{36} and one β-B_{34} in a $\sqrt{3} \times \sqrt{3}$ super lattice. Note that each β-B_{34} cluster is surrounded by B_{36} clusters, which provides a criterion of prejudging the semiconducting characteristics. Based on our calculations, the monolayer is probably semiconducting when β-B_{34} clusters are almost surrounded by B_{36} clusters; otherwise, it is metallic. To investigate the thermodynamic properties, we selected a supercell of 424 atoms and performed the AIMD simulation. According to the time-average magnetic moment at finite temperatures (each over 5 ps), the magnetic moment still does not vanish above room temperature of 400 K, indicating that the magnetic moment can still exist steadily above room temperature. Note that the DFT calculations can tell us the magnetic moment and band gap in each step of AMID, and therefore, we performed 10 000 steps (10 fs) of AIMD; the mean magnetic moment is calculated by the time average of the last 1000 steps. Similarly, we estimated the average band gap based on AIMD with a given temperature, which is the result of the atomic deviation. The detailed discussion can be found in the section Band gap and magnetic moment at finite temperature of the ESI.† The spin-polarized band structure of MS-boron is shown in Fig. 7b and c, with a band gap of 0.24 eV (majority spin) and 0.28 eV (minority spin), respectively. The orbital resolved characteristics of energy bands show a predominant contribution of the p_z orbital in the VBM and the CBM, indi-

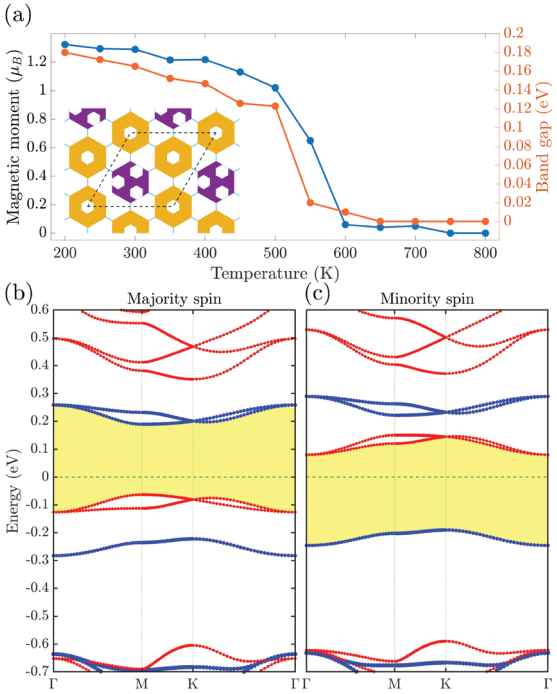

Fig. 7 (a) The magnetic moment and band gap vary with the temperature under AIMD simulation. (b and c) The orbital resolved band structure of MS-boron at the majority and minority spin states, respectively. The red and blue energy bands represent the contribution of the p_z and $p_x + p_y$ orbitals.

cating that the spin-polarized state is generated by π-electrons. The gap between the VBM and CBM will vanish at high temperatures, indicating that the FM and semiconducting characteristics will be maintained below 500 K, as shown in Fig. 7a.

4 Conclusion

In summary, we have theoretically predicted a hierarchy of magnetic boron nanostructures based on the first-principles calculations. It has been demonstrated that the FM induced by p electrons will occur in an all-boron planar cluster, in which the structural symmetry is dominant to the number of unpaired electrons. Strikingly, there are six radicals in the α-B_{34} cluster, which can be further assembled into ferromagnetic monolayers with $2\mu_B$–$3\mu_B$ per cluster. With the hybridization of β-B_{34} and B_{36} clusters observed in the previous experiment, the assembled monolayers can even exhibit magnetic semiconducting characteristics with a maximum band gap of 0.18 eV and a magnetic moment of $0.68\mu_B$ per cluster. According to the *ab initio* molecular dynamics simulation, the FM and magnetic semiconducting characteristics in boron monolayers are robust and will be maintained at room temperature, serving as a promising candidate for applications in nanoelectronic and spintronic devices once they can be synthesized experimentally.

Conflicts of interest

There are no conflicts to declare.

Acknowledgements

This work was supported by the National Natural Science Foundation of China (No. 11974160), the Guangdong Natural Science Funds for Distinguished Young Scholars (No. 2017B030306008), the Guangdong Provincial Key Laboratory of Computational Science and Material Design (No. 2019B030301001), the Guangdong–Hong Kong–Macao Joint Laboratory (No. 2019B121205001), and the Key-Area Research and Development Program of Guangdong Province (No. 2020B010183001). The computer time at the Center for Computational Science and Engineering of Southern University of Science and Technology is gratefully acknowledged.

References

1 I. Žutić, J. Fabian and S. Das Sarma, *Rev. Mod. Phys.*, 2004, **76**, 323–410.
2 P. A. Lee, N. Nagaosa and X.-G. Wen, *Rev. Mod. Phys.*, 2006, **78**, 17–85.
3 F. Hellman, A. Hoffmann, Y. Tserkovnyak, G. S. D. Beach, E. E. Fullerton, C. Leighton, A. H. MacDonald, D. C. Ralph, D. A. Arena, H. A. Dürr, P. Fischer, J. Grollier, J. P. Heremans, T. Jungwirth, A. V. Kimel, B. Koopmans, I. N. Krivorotov, S. J. May, A. K. Petford-Long, J. M. Rondinelli, N. Samarth, I. K. Schuller, A. N. Slavin, M. D. Stiles, O. Tchernyshyov, A. Thiaville and B. L. Zink, *Rev. Mod. Phys.*, 2017, **89**, 025006.
4 E. Coronado, *Nat. Rev. Mater.*, 2020, **5**, 87–104.
5 S. Wolf, D. Awschalom, R. Buhrman, J. Daughton, S. von Molnar, M. Roukes, A. Chtchelkanova and D. Treger, *Science*, 2001, **294**, 1488–1495.
6 H. Ohldag, T. Tyliszczak, R. Höhne, D. Spemann, P. Esquinazi, M. Ungureanu and T. Butz, *Phys. Rev. Lett.*, 2007, **98**, 187204.
7 W. L. Wang, O. V. Yazyev, S. Meng and E. Kaxiras, *Phys. Rev. Lett.*, 2009, **102**, 157201.
8 R. Ortiz, R. A. Boto, N. García-Martínez, J. C. Sancho-García, M. Melle-Franco and J. Fernández-Rossier, *Nano Lett.*, 2019, **19**, 5991–5997.
9 S. Mishra, D. Beyer, K. Eimre, J. Liu, R. Berger, O. Gröning, C. A. Pignedoli, K. Müllen, R. Fasel, X. Feng and P. Ruffieux, *J. Am. Chem. Soc.*, 2019, **141**, 10621–10625.
10 J. Su, M. Telychko, P. Hu, G. Macam, P. Mutombo, H. Zhang, Y. Bao, F. Cheng, Z.-Q. Huang, Z. Qiu, S. J. R. Tan, H. Lin, P. Jelínek, F.-C. Chuang, J. Wu and J. Lu, *Sci. Adv.*, 2019, **5**, eaav7717.
11 J. Li, S. Sanz, J. Castro-Esteban, M. Vilas-Varela, N. Friedrich, T. Frederiksen, D. Peña and J. I. Pascual, *Phys. Rev. Lett.*, 2020, **124**, 177201.

12 S. Mishra, D. Beyer, R. Berger, J. Liu, O. Gröning, J. I. Urgel, K. Müllen, P. Ruffieux, X. Feng and R. Fasel, *J. Am. Chem. Soc.*, 2020, **142**, 1147–1152.
13 Y. Zheng, C. Li, Y. Zhao, D. Beyer, G. Wang, C. Xu, X. Yue, Y. Chen, D.-D. Guan, Y.-Y. Li, H. Zheng, C. Liu, W. Luo, X. Feng, S. Wang and J. Jia, *Phys. Rev. Lett.*, 2020, **124**, 147206.
14 A. Du, S. Sanvito and S. C. Smith, *Phys. Rev. Lett.*, 2012, **108**, 197207.
15 X. Zhang, X. Xie, H. Wang, J. Zhang, B. Pan and Y. Xie, *J. Am. Chem. Soc.*, 2013, **135**, 18–21.
16 X. Li, J. Zhou, Q. Wang, Y. Kawazoe and P. Jena, *J. Phys. Chem. Lett.*, 2013, **4**, 259–263.
17 A. Bafekry, M. Neek-Amal and F. M. Peeters, *Phys. Rev. B*, 2020, **101**, 165407.
18 B. Albert and H. Hillebrecht, *Angew. Chem., Int. Ed.*, 2009, **48**, 8640–8668.
19 Z. Zhang, E. S. Penev and B. I. Yakobson, *Chem. Soc. Rev.*, 2017, **46**, 6746–6763.
20 Z. A. Piazza, H.-S. Hu, W.-L. Li, Y.-F. Zhao, J. Li and L.-S. Wang, *Nat. Commun.*, 2014, **5**, 3113.
21 T. B. Tai and M. T. Nguyen, *Phys. Chem. Chem. Phys.*, 2015, **17**, 13672–13679.
22 Q. Chen, W.-J. Tian, L.-Y. Feng, H.-G. Lu, Y.-W. Mu, H.-J. Zhai, S.-D. Li and L.-S. Wang, *Nanoscale*, 2017, **9**, 4550–4557.
23 Q. Chen, T.-T. Chen, H.-R. Li, X.-Y. Zhao, W.-J. Chen, H.-J. Zhai, S.-D. Li and L.-S. Wang, *Nanoscale*, 2019, **11**, 9698–9704.
24 T. Jian, X. Chen, S.-D. Li, A. I. Boldyrev, J. Li and L.-S. Wang, *Chem. Soc. Rev.*, 2019, **48**, 3550–3591.
25 B. Feng, J. Zhang, Q. Zhong, W. Li, S. Li, H. Li, P. Cheng, S. Meng, L. Chen and K. Wu, *Nat. Chem.*, 2016, **8**, 563–568.
26 X.-F. Zhou, X. Dong, A. R. Oganov, Q. Zhu, Y. Tian and H.-T. Wang, *Phys. Rev. Lett.*, 2014, **112**, 085502.
27 E. S. Penev, A. Kutana and B. I. Yakobson, *Nano Lett.*, 2016, **16**, 2522–2526.
28 S.-G. Xu, X.-T. Li, Y.-J. Zhao, J.-H. Liao, W.-P. Xu, X.-B. Yang and H. Xu, *J. Am. Chem. Soc.*, 2017, **139**, 17233–17236.
29 X.-F. Zhou, A. R. Oganov, Z. Wang, I. A. Popov, A. I. Boldyrev and H.-T. Wang, *Phys. Rev. B*, 2016, **93**, 085406.
30 M.-H. Zhu, X.-J. Weng, G. Gao, S. Dong, L.-F. Lin, W.-H. Wang, Q. Zhu, A. R. Oganov, X. Dong, Y. Tian, X.-F. Zhou and H.-T. Wang, *Phys. Rev. B*, 2019, **99**, 205412.
31 N. V. Tkachenko, D. Steglenko, N. Fedik, N. M. Boldyreva, R. M. Minyaev, V. I. Minkin and A. I. Boldyrev, *Phys. Chem. Chem. Phys.*, 2019, **21**, 19764–19771.
32 S.-G. Xu, Y.-J. Zhao, J.-H. Liao and X.-B. Yang, *J. Chem. Phys.*, 2015, **142**, 214307.
33 G. Kresse and J. Furthmüller, *Phys. Rev. B: Condens. Matter Mater. Phys.*, 1996, **54**, 11169–11186.
34 G. Kresse and D. Joubert, *Phys. Rev. B: Condens. Matter Mater. Phys.*, 1999, **59**, 1758–1775.
35 J. P. Perdew, K. Burke and M. Ernzerhof, *Phys. Rev. Lett.*, 1996, **77**, 3865–3868.
36 J. P. Perdew, K. Burke and M. Ernzerhof, *Phys. Rev. Lett.*, 1998, **80**, 891–891.
37 J. Paier, M. Marsman, K. Hummer, G. Kresse, I. C. Gerber and J. G. Ángyán, *J. Chem. Phys.*, 2006, **124**, 154709.
38 J. Heyd, G. E. Scuseria and M. Ernzerhof, *J. Chem. Phys.*, 2003, **118**, 8207–8215.
39 A. Togo and I. Tanaka, *Scr. Mater.*, 2015, **108**, 1–5.
40 H. Bai, T.-T. Chen, Q. Chen, X.-Y. Zhao, Y.-Y. Zhang, W.-J. Chen, W.-L. Li, L. F. Cheung, B. Bai, J. Cavanagh, W. Huang, S.-D. Li, J. Li and L.-S. Wang, *Nanoscale*, 2019, **11**, 23286–23295.
41 C.-C. He, S.-B. Qiu, J.-S. Yu, J.-H. Liao, Y.-J. Zhao and X.-B. Yang, *J. Phys. Chem. A*, 2020, **124**, 4506–4511.
42 M. Kabir and T. Saha-Dasgupta, *Phys. Rev. B: Condens. Matter Mater. Phys.*, 2014, **90**, 035403.
43 J. Fernández-Rossier and J. J. Palacios, *Phys. Rev. Lett.*, 2007, **99**, 177204.
44 Q. Chen, W.-L. Li, X.-Y. Zhao, H.-R. Li, L.-Y. Feng, H.-J. Zhai, S.-D. Li and L.-S. Wang, *Eur. J. Inorg. Chem.*, 2017, **2017**, 4546–4551.
45 X. Sun, X. Liu, J. Yin, J. Yu, Y. Li, Y. Hang, X. Zhou, M. Yu, J. Li, G. Tai and W. Guo, *Adv. Funct. Mater.*, 2017, **27**, 1603300.
46 S.-G. Xu, Y.-J. Zhao, X.-B. Yang and H. Xu, *J. Phys. Chem. C*, 2017, **121**, 11950–11955.
47 G. Henkelman, B. P. Uberuaga and H. Jónsson, *J. Chem. Phys.*, 2000, **113**, 9901–9904.
48 X. Wu, J. Dai, Y. Zhao, Z. Zhuo, J. Yang and X. C. Zeng, *ACS Nano*, 2012, **6**, 7443–7453.